INTERNATIONAL JOURNAL FOR NUMERICAL METHODS IN FLUIDS, VOL. 24, 1433–1448 (1997)

SIMULATION OF FLOW PROBLEMS WITH MOVING MECHANICAL COMPONENTS, FLUID–STRUCTURE INTERACTIONS AND TWO-FLUID INTERFACES

G. P. WREN,[1,*] S. E. RAY,[1,2] S. K. ALIABADI[2] AND T. E. TEZDUYAR[2]

[1] *Weapons and Materials Research Directorate, U.S. Army Research Laboratory, Aberdeen Proving Ground, MD 21005-5066, U.S.A.*

[2] *Department of Aerospace Engineering and Mechanics, Army High Performance Computing Research Center, University of Minnesota, 1100 Washington Avenue South, Minneapolis, MN 55415, U.S.A.*

SUMMARY

The application of a stabilized space–time finite element formulation to problems involving fluid–structure interactions and two-fluid interfaces is discussed. Two sample problems are presented and the method is validated by comparison with a test problem. Ⓒ1997 by John Wiley & Sons, Ltd.

Int. J. Numer. Meth. Fluids, **24**: 1433–1448, 1997

No. of Figures: 10. No. of Tables: 0. No. of References: 30.

KEY WORDS: flow simulation; moving mechanical components; fluid-structure interactions; two-fluid interfaces

1. INTRODUCTION

Increasingly, problems of interior ballistics for advanced gun systems are treated as multidisciplinary in nature, since the flow fields are stressed beyond traditional limits in physical parameters such as pressures and temperatures. The gun internal environment for tank and artillery is by nature severe: ranging in pressure from ambient to 500 MPa or higher; temperatures from ambient to the flame temperature of the solid propellant up to 3500 K; acceleration of tactical projectiles with intruding afterbodies to muzzle velocities exceeding 2500 m s^{-1}; all within the timeframe of 25 ms. However, advanced gun systems exceed these limits in order to achieve greater muzzle kinetic energies and, at the same time, often introduce additional complexity associated with liquid propellants and electrical energy. For example, although the regenerative liquid propellant gun is within traditional limits in terms of pressures and temperatures, it utilizes moving mechanical pistons to inject liquid propellant from a reservoir into the combustion chamber. Since the pistons move, the combustion chamber shape and volume change in time. In the electrothermal–chemical gun, electrical energy in the form of a plasma is injected into the combustion chamber, raising the temperature at least locally to as high as 20,000 K.

Experimental data have suggested an interaction between diverse media in the gun. For example, pistons used in the regenerative liquid propellant gun and the flow field interact both to deform the pistons and to influence the fluid flow from the reservoir into the combustion chamber. Break-up of the fluid into droplets both during high-velocity injection into gas, and in regions in which a puddle of liquid is impacted by a high-velocity jet of gas, is caused by shear stress between the liquid and the

*Correspondence to: G.P. Wren, U.S. Army Research Laboratory, Aberdeen Proving Ground, MD 21005-5066, U.S.A.

CCC 0271–2091/97/121433–16 $17.50 *Received 15 April 1996*

Revised 12 July 1996

gas. Long-body projectiles which intrude into the combustion chamber, such as those used for kinetic energy weapons, respond to the flow fields of electrothermal–chemical guns and advanced charge designs uniquely differently from the response in traditional guns. Thus new computational techniques are needed to address coupling problems of interior ballistics which involve interaction between diverse media such as gases, deformable solids and liquids.

The most promising computational method for the solution of interaction problems between diverse media with complex geometries is the finite element method using formulations for multiphase, multicomponent, compressible, reacting fluid flow with real equations of state. The development of finite element formulations for fluid dynamics applications is a research field that offers significant promise for such difficult problems. In this paper we utilize the deformable-spatial-domain/stabilized-space–time (DST/SST) finite element formulation to study a multifluid, non-reacting, compressible and incompressible flow problem in which a slightly compressible barotropic liquid interacts with an incompressible gas. We also couple the DSD/SST-based model of the barotropic liquid with a finite element model of a linearly elastic body to study fluid–structure interaction phenomena.

In a discontinuous-in-time space–time formulation the governing equations of the problem are integrated in the space–time domain. Also, the finite element interpolation functions are functions of both spatial location and time. These interpolation functions are discontinuous in time but continuous in space. Discontinuous-in-time space–time methods were earlier used with spatial domains which do not change with time.[1–4]

The DSD/SST formulation takes advantage of the fact that the governing equations are integrated over the space–time domain, by being able to absorb mesh deformation automatically in problems involving moving boundaries and interfaces. This method was first introduced for incompressible flows.[5] Later, a similar technique was developed for compressible flows.[6] The DSD/SST formulation can be effectively implemented on parallel supercomputers.[7–9]

Two types of stabilization techniques are used in the DSD/SST finite element formulations. For compressible flows the DSD/SST formulation, which is in the context of conservation variables, is stabilized using the streamline-upwind/Petrov–Galerkin (SUPG) method. The SUPG method for incompressible flows was first introduced by Hughes and Brooks,[10] with a detailed description of the formulation and numerical examples given in Reference 11. The SUPG method for compressible flows, in the context of conservation variables, was introduced by Tezduyar and Hughes.[12] Later, this method for compressible flows was refined and studied by several researchers.[13–17] The DSD/SST finite element formulation for incompressible flows is stabilised using the Galerkin/least-squares (GLS) method.[18,19] One can view the GLS method as a generalization of the SUPG method. For the details of the GLS method see Reference 3.

In problems involving moving components, or two-fluid problems in which tracking of the interface is necessary, the mesh deforms in response to domain boundary and interface movement. An automatic mesh-moving scheme[20,21] is employed to take into account the mesh deformation. Occasionally the mesh distortion grows and an automatic mesh generator[22] is used to periodically generate a new mesh in order to limit the deformation of the mesh.

In this paper we review the governing equations and solution for three interaction problems: (i) the vibration of a metal plate in a vacuum and also with a fluid on one side; (ii) the interaction between a compressible fluid and a piston treated as an electric body; (iii) the interaction between a jet of gas and a puddle of liquid. In Section 2 we discuss the governing equations for incompressible and compressible flows and for linear elastodynamics. In Section 3 we discuss the finite element formulations used in this work and the interface conditions used in modelling the multimedia interaction. These methods are tested on three problems, presented in Section 4, and conclusions are presented in Section 5.

2. GOVERNING EQUATIONS

Let $\Omega_t \subset \mathbb{R}^{n_{sd}}$ and $(0, T)$ be the spatial and temporal domains respectively, where n_{sd} is the number of space dimensions, and let Γ_t denote the boundary of Ω_t. The subscript t implies the time dependence of the spatial domain. The spatial and temporal co-ordinates are denoted by $\mathbf{x} \in \Omega_t$ and $t \in (0, T)$.

2.1. Incompressible flows

The Navier–Stokes equations for incompressible flows are

$$\rho\left(\frac{\partial \mathbf{u}}{\partial t} + \mathbf{u} \cdot \nabla \mathbf{u} - \mathbf{f}\right) - \nabla \cdot \boldsymbol{\sigma} = \mathbf{0} \quad \text{on } \Omega_t, \tag{1}$$

$$\nabla \cdot \mathbf{u} = 0 \quad \text{on } \Omega_t, \tag{2}$$

where ρ is the density $\mathbf{u}$ is the velocity vector and $\mathbf{f}$ is the body force per unit mass. For the Newtonian fluids under consideration the stress tensor for a fluid with dynamic viscosity μ is defined as

$$\boldsymbol{\sigma}(\mathbf{u}, p) = -p\mathbf{I} + 2\mu\boldsymbol{\epsilon}(\mathbf{u}), \tag{3}$$

where $\mathbf{I}$ is the identity tensor and p denotes the pressure. The strain rate tensor is defined as

$$\boldsymbol{\epsilon}(\mathbf{u}) = \tfrac{1}{2}[\nabla \mathbf{u} + (\nabla \mathbf{u})^{\mathrm{T}}]. \tag{4}$$

The Dirichlet- and Neumann-type boundary conditions are represented respectively as

$$\begin{aligned} \mathbf{u} &= \mathbf{g} \quad \text{on } (\Gamma_t)_g, \\ \mathbf{n} \cdot \boldsymbol{\sigma} &= \mathbf{h} \quad \text{on } (\Gamma_t)_h, \end{aligned} \tag{5}$$

where $(\Gamma_t)_g$ and $(\Gamma_t)_h$ are complementary subsets of the boundary Γ_t. The initial condition on the velocity is specified on Ω_0:

$$\mathbf{u}(\mathbf{x}, 0) = \mathbf{u}_0 \quad \text{on } \Omega_0, \tag{6}$$

where $\mathbf{u}_0$ is divergence-free.

2.2. Compressible liquid flows

Compressibility of liquids is measured in terms of the bulk modulus, which gives the variation in pressure for a fractional change in density at a constant temperature, i.e.

$$K = \rho\left(\frac{\partial p}{\partial \rho}\right)_\theta. \tag{7}$$

Here K and θ are the bulk modulus and temperature respectively. For liquids the bulk modulus is typically very large (in the range of billions of Pascals in our case), meaning that the compressibility is very small. In problems with the pressure of the same order of magnitude as the bulk modulus, the compressibility of the working fluid plays an important role. Although the variations in density are small, these still lead to large variations in pressure. In such cases the liquid is usually modelled as a barotropic fluid, in which the pressure is assumed to be a function of density alone. A simple equation of state which relates the pressure to the density can be obtained by assuming that the bulk modulus is a linear function of pressure, i.e.

$$K = K_1 + K_2 p, \tag{8}$$

where K_1 is the bulk modulus at zero gauge pressure and K_2 is a dimensionless constant. The solution of equations (7) and (8) yields

$$p = \frac{K_1}{K_2}\left[\left(\frac{\rho}{\rho_0}\right)^{K_2} - 1\right], \tag{9}$$

where ρ_0 is the density at zero gauge pressure.

The barotropic fluid assumption, along with the assumption of constant viscosity, decouples the energy equation from the governing equations, and the equations of conservation of mass and momentum suffice to describe the flow field characteristics of compressible liquid flows. These equations in conservation law form can be written as

$$\frac{\partial \mathbf{U}}{\partial t} + \frac{\partial \mathbf{F}_i}{\partial x_i} - \frac{\partial \mathbf{E}_i}{\partial x_i} = \mathbf{0} \quad \text{on } \Omega_t, \tag{10}$$

where $\mathbf{U} = (\rho, \rho u_1, \rho u_2, \rho u_3)$ is the vector of conservation variables and $\mathbf{F}_i$ and $\mathbf{E}_i$ are respectively the Euler and viscous flux vectors defined as

$$\mathbf{F}_i = \begin{pmatrix} u_i \rho \\ u_i \rho u_1 + \delta_{i1} p \\ u_i \rho u_2 + \delta_{i2} p \\ u_i \rho u_3 + \delta_{i3} p \end{pmatrix}, \tag{11}$$

$$\mathbf{E}_i = \begin{pmatrix} 0 \\ [\mathbf{T}]_{i1} \\ [\mathbf{T}]_{i2} \\ [\mathbf{T}]_{i3} \end{pmatrix}. \tag{12}$$

Here the identity tensor is denoted by δ_{ij} and $[\mathbf{T}]_{ij}$ are the components of the viscous stress tensor $\mathbf{T}$ defined as

$$\mathbf{T} = \mu[\nabla \mathbf{u} + (\nabla \mathbf{u})^{\mathrm{T}}] - \tfrac{2}{3}\mu(\nabla \cdot \mathbf{u})\mathbf{I}. \tag{13}$$

Alternatively, equation (10) can be written as

$$\frac{\partial \mathbf{U}}{\partial t} + \mathbf{A}_i \frac{\partial \mathbf{U}}{\partial x_i} - \frac{\partial}{\partial x_i}\left(\mathbf{K}_{ij} \frac{\partial \mathbf{U}}{\partial x_j}\right) = \mathbf{0} \quad \text{on } \Omega_t, \tag{14}$$

where

$$\mathbf{A}_i = \frac{\partial \mathbf{F}_i}{\partial \mathbf{U}}, \tag{15}$$

$$\mathbf{K}_{ij} \frac{\partial \mathbf{U}}{\partial x_j} = \mathbf{E}_i. \tag{16}$$

An appropriate set of boundary and initial conditions is assumed to accompany equation (14).

In the fluid–structure interaction computations the assumption of axisymmetry is used. Under this assumption the equations of conservation of mass and momentum are written as

$$\frac{\partial \mathbf{U}}{\partial t} + \frac{\partial \mathbf{F}_z}{\partial z} + \frac{\partial \mathbf{F}_r}{\partial r} + \mathbf{S}_r - \nabla \cdot \mathbf{E} = \mathbf{0} \quad \text{on } \Omega_t, \tag{17}$$

where r and z are the radial and axial co-ordinates respectively. The vector of conservation variables and the Euler flux vectors are

$$\mathbf{U} = \begin{pmatrix} \rho \\ \rho u_z \\ \rho u_r \end{pmatrix}, \qquad \mathbf{F}_z = \begin{pmatrix} u_z \rho \\ u_z \rho u_z + p \\ u_z \rho u_r \end{pmatrix}, \qquad \mathbf{F}_r = \begin{pmatrix} u_r \rho \\ u_r \rho u_z \\ u_r \rho u_r + p \end{pmatrix}. \tag{18}$$

Also

$$\mathbf{S}_r = \frac{u_r}{r}\mathbf{U}. \tag{19}$$

$\mathbf{E}$ is the matrix containing the dissipative terms:

$$\mathbf{E} = \begin{pmatrix} \mathbf{0} \\ \mathbf{T} \end{pmatrix}. \tag{20}$$

Equation (17) can also be written as

$$\frac{\partial \mathbf{U}}{\partial t} + \mathbf{A}_z \frac{\partial \mathbf{U}}{\partial z} + \mathbf{A}_r \frac{\partial \mathbf{U}}{\partial r} + \mathbf{S}_r - \nabla \cdot \mathbf{E} = \mathbf{0} \quad \text{on } \Omega_f. \tag{21}$$

$\mathbf{A}_z$ and $\mathbf{A}_r$ are the Jacobians of the Euler flux vectors with respect to $\mathbf{U}$:

$$\mathbf{A}_z = \frac{\partial \mathbf{F}_z}{\partial \mathbf{U}}, \qquad \mathbf{A}_r = \frac{\partial \mathbf{F}_r}{\partial \mathbf{U}}. \tag{22}$$

Again, appropriate boundary and initial conditions are specified for equation (21).

2.3. Linear Elastodynamics

The deformations studied in this research are assumed to be small enough to be considered elastic. The motion and deformation of the solid can therefore be described using classical linear elasticity theory and the governing equations are

$$\rho_s \ddot{\mathbf{d}} = \nabla \cdot \boldsymbol{\sigma}_s + \mathbf{b} \quad \text{on } \Omega_s. \tag{23}$$

ρ_s is the density of the solid and $\mathbf{d}, \dot{\mathbf{d}}$ and $\ddot{\mathbf{d}}$ are the displacement, velocity and acceleration respectively of a point in the body. $\boldsymbol{\sigma}_s$ is the Cauchy stress tensor in the solid. The body force $\mathbf{b}$ is assumed to be zero throughout this work.

If the body is assumed to be homogeneous and isotropic, $\boldsymbol{\sigma}_s$ can be written[23] as

$$\boldsymbol{\sigma}_s = \mu_s[\nabla \mathbf{d} + (\nabla \mathbf{d})^T] + \lambda_s(\nabla \cdot \mathbf{d})\mathbf{I}, \tag{24}$$

where λ_s and μ_s are Lame's elastic constants and μ_s is sometimes called the shear modulus and denoted by G. They are related to Young's modulus E_s and Poisson's ratio ν_s by

$$\lambda_s = \frac{\nu_s E_s}{(1+\nu_s)(1-2\nu_s)}, \tag{25}$$

$$\mu_s = \frac{E_s}{2(1+\nu_s)}. \tag{26}$$

The Dirichlet and Neumann boundary conditions are written as

$$\mathbf{d} = \mathbf{g}_s \quad \text{on } [\Gamma_s]_g \times (0, T), \tag{27}$$

$$\mathbf{n} \cdot \boldsymbol{\sigma}_s = \mathbf{h}_s \quad \text{on } [\Gamma_s]_h \times (0, T). \tag{28}$$

$[\Gamma_s]_g$ and $[\Gamma_s]_h$ are complementary subsets of the boundary Γ_s. The initial conditions are

$$\mathbf{d}(\mathbf{x},0)=\mathbf{d}_0 \quad \text{on } \Omega_s, \tag{29}$$

$$\dot{\mathbf{d}}(\mathbf{x},0)=\dot{\mathbf{d}}_0 \quad \text{on } \Omega_s. \tag{30}$$

There must also be conditions defined on the fluid–structure interface. These are that the fluid does not slip along the structure surface. Also, the only fluid force assumed to act upon the structure is the pressure force, since this is assumed to be much larger than the viscous forces.

3. DSD/SST FORMULATION

3.1. Incompressible flows

In order to construct the finite element function spaces for the space–time method, we partition the time interval $(0, T)$ into subintervals $I_n=(t_n, t_{n+1})$, where t_n and t_{n+1} belong to an ordered series of time levels $0=t_0<t_1<\cdots<t_N=T$. Let $\Omega_n=\Omega_{t_n}$ and $\Gamma_n=\Gamma_{t_n}$. We define the space–time slab Q_n as the domain enclosed by the surfaces Ω_n, Ω_{n+1} and P_n, where P_n is the surface described by the boundary Γ_t as t traverses I_n. As is the case with Γ_t, the surface P_n is decomposed into $(P_n)_g$ and $(P_n)_h$ with respect to the type of boundary condition (Dirichlet or Neumann) being imposed. For each space–time slab we define the corresponding finite element function spaces $(\mathscr{S}^h_{\mathbf{u}})_n$, $(\mathscr{V}^h_{\mathbf{u}})_n$, $(\mathscr{S}^h_p)_n$ and $(\mathscr{V}^h_p)_n$. Over the element domain this space is formed by using first-order polynomials in space and time. Globally, the interpolation functions are continuous in space but discontinuous in time.

The stabilized space–time formulation for deforming domains is then written as follows: given $(\mathbf{u}^h)_n^-$, find $\mathbf{u}^h\in(\mathscr{S}^h_{\mathbf{u}})_n$ and $p^h\in(\mathscr{S}^h_p)_n$ such that $\forall \mathbf{w}^h\in(\mathscr{V}^h_{\mathbf{u}})_n$ and $q^h\in(\mathscr{V}^h_p)_n$

$$\begin{aligned}
&\int_{Q_n}\mathbf{w}^h\cdot\rho\left(\frac{\partial\mathbf{u}^h}{\partial t}+\mathbf{u}^h\cdot\nabla\mathbf{u}^h-\mathbf{f}^h\right)\mathrm{d}Q+\int_{Q_n}\boldsymbol{\epsilon}(\mathbf{w}^h):\boldsymbol{\sigma}(p^h,\mathbf{u}^h)\mathrm{d}Q+\int_{Q_n}q^h\nabla\cdot\mathbf{u}^h\mathrm{d}Q\\
&\quad+\sum_{e=1}^{n_{\mathrm{el}}}\int_{Q_n^e}\frac{1}{\rho}\tau\left[\rho\left(\frac{\partial\mathbf{w}^h}{\partial t}+\mathbf{u}^h\cdot\nabla\mathbf{w}^h\right)+\nabla q^h-2\mu\nabla\cdot\boldsymbol{\epsilon}(\mathbf{w}^h)\right]\\
&\quad\cdot\left[\rho\left(\frac{\partial\mathbf{u}^h}{\partial t}+\mathbf{u}^h\cdot\nabla\mathbf{u}^h-\mathbf{f}^h\right)+\nabla p^h-2\mu\nabla\cdot\boldsymbol{\epsilon}(\mathbf{u}^h)\right]\mathrm{d}Q+\sum_{e=1}^{n_{\mathrm{el}}}\int_{Q_n^e}\delta\nabla\cdot\mathbf{w}^h\rho\nabla\cdot\mathbf{u}^h\mathrm{d}Q\\
&\quad+\int_{\Omega_n}(\mathbf{w}^h)_n^+\cdot\rho[(\mathbf{u}^h)_n^+-(\mathbf{u}^h)_n^-]\,\mathrm{d}\Omega=\int_{(P_n)_h}\mathbf{w}^h\cdot\mathbf{h}^h\mathrm{d}P
\end{aligned} \tag{31}$$

This process is applied sequentially to all the space–time slabs $Q_0, Q_1, \ldots, Q_{N-1}$. In the variational formulation given by equation (31), the following notation is used:

$$(\mathbf{u}^h)_n^{\pm}=\lim_{\epsilon\to 0}\mathbf{u}(t_n\pm\epsilon), \tag{32}$$

$$\int_{Q_n}(\ldots)\mathrm{d}Q=\int_{I_n}\int_{\Omega_n}(\ldots)\mathrm{d}\Omega\mathrm{d}t, \tag{33}$$

$$\int_{P_n}(\ldots)\mathrm{d}P=\int_{I_n}\int_{\Gamma_n}(\ldots)\mathrm{d}\Gamma\mathrm{d}t. \tag{34}$$

The computations start with

$$(\mathbf{u}^h)_0^-=\mathbf{u}_0^h. \tag{35}$$

In the variational formulation given by equation (31), the first three terms and the right-hand side constitute the Galerkin formulation of the problem. The first series of element-level integrals in

equation (31) consists of least squares terms based on the momentum equation. The second series of element-level integrals is added to the formulation for numerical stability at high Reynolds numbers; these are least squares terms based on the continuity equation. Both stabilization terms are weighted residuals and therefore maintain the consistency of the formulation. The sixth term enforces, weakly, the continuity of the velocity field between the space–time slabs. The stabilization coefficients τ and δ are defined in References 5 and 24.

3.2. Compressible flows

In the finite element formulation of compressible flows we define the function spaces $\mathscr{S}_n^h$ and $\mathscr{V}_n^h$ corresponding to the trial solutions and weighting functions respectively. Again we use first-order polynomials as interpolation functions. Globally, these functions are continuous in space but discontinuous in time.

The DSD/SST formulation of (14) can be written as follows: given $(\mathbf{U}^h)_n^-$, find $\mathbf{U}^h \in \mathscr{S}_n^h$ such that $\forall \mathbf{W}^h \in \mathscr{V}_n^h$

$$\begin{aligned}
&\int_{Q_n} \mathbf{W}^h \cdot \left(\frac{\partial \mathbf{U}^h}{\partial t} + \mathbf{A}_i^h \frac{\partial \mathbf{U}^h}{\partial x_i} \right) \mathrm{d}Q + \int_{Q_n} \left(\frac{\partial \mathbf{W}^h}{\partial x_i} \right) \cdot \left(\mathbf{K}_{ij}^h \frac{\partial \mathbf{U}^h}{\partial x_j} \right) \mathrm{d}Q + \int_{\Omega_n} (\mathbf{W}^h)_n^+ \cdot [(\mathbf{U}^h)_n^+ - (\mathbf{U}^h)_n^-] \, \mathrm{d}\Omega \\
&\quad + \sum_{e=1}^{(n_{\mathrm{el}})_n} \int_{Q_n^e} \boldsymbol{\tau} (\mathbf{A}_k^h)^{\mathrm{T}} \left(\frac{\partial \mathbf{W}^h}{\partial x_k} \right) \cdot \left(\frac{\partial \mathbf{U}^h}{\partial t} + \mathbf{A}_i^h \frac{\partial \mathbf{U}^h}{\partial x_i} \right) \mathrm{d}Q + \sum_{e=1}^{(n_{\mathrm{el}})_n} \int_{Q_n^e} \delta \left(\frac{\partial \mathbf{W}^h}{\partial x_i} \right) \cdot \left(\frac{\partial \mathbf{U}^h}{\partial x_i} \right) \mathrm{d}Q \\
&\quad = \int_{(P_n)_{\mathrm{H}}} \mathbf{W}^h \cdot \mathbf{H}^h \, \mathrm{d}P. \qquad (36)
\end{aligned}$$

where $\mathbf{H}$ is the Neumann-type boundary condition, and $(P_n)_{\mathrm{H}}$ is the part of the space-time boundary with such boundary condition.

The solution to (36) is obtained sequentially for $Q_0, Q_1, \ldots, Q_{N-1}$, commencing with

$$(\mathbf{U}^h)_0^- = \mathbf{U}_0^h, \qquad (37)$$

where $\mathbf{U}_0$ is the initial value of the vector $\mathbf{U}$. The notation given in equations (32)–(34) is also used in equation (36).

In the formulation (36) the first three integrals together with the right-hand side represent the time-discontinuous Galerkin formulation of (14). The third integral enforces, weakly, the continuity of the conservation variables in time. The first series of element-level integrals consists of the SUPG stabilization terms and the second series consists of the shock-capturing terms added to the formulation. The definitions of $\boldsymbol{\tau}$, a diagonal matrix, and δ are given in Reference 6.

Once again, assuming axisymmetry, the DSD/SST formulation of equation (21) can be written as follows: given $(\mathbf{U}^h)_n^-$, find $\mathbf{U}_h \in \mathscr{S}_n^h$ such that $\forall \mathbf{W}^h \in \mathscr{V}_n^h$

$$\begin{aligned}
&\int_{Q_n} \mathbf{W}^h \cdot \left(\frac{\partial \mathbf{U}^h}{\partial t} + \mathbf{A}_z^h \frac{\partial \mathbf{U}^h}{\partial z} + \mathbf{A}_r^h \frac{\partial \mathbf{U}^h}{\partial r} + \mathbf{S}_r^h \right) \mathrm{d}Q + \int_{Q_n} \nabla \mathbf{W}^h : \mathbf{E}^h \, \mathrm{d}Q + \int_{\Omega_n} (\mathbf{W}^h)_n^+ \cdot [(\mathbf{U}^h)_n^+ \\
&\quad - (\mathbf{U}^h)_n^-] \mathrm{d}\Omega + \sum_{e=1}^{(n_{\mathrm{el}})_n} \int_{Q_n^e} \left((\mathbf{A}_z^h)^{\mathrm{T}} \frac{\partial \mathbf{W}^h}{\partial z} + (\mathbf{A}_r^h)^{\mathrm{T}} \frac{\partial \mathbf{W}^h}{\partial r} \right) \cdot \left(\frac{\partial \mathbf{U}^h}{\partial t} + \mathbf{A}_z^h \frac{\partial \mathbf{U}^h}{\partial z} + \mathbf{A}_r^h \frac{\partial \mathbf{U}^h}{\partial r} + \mathbf{S}_r^h \right) \mathrm{d}Q \\
&\quad + \sum_{e=1}^{(n_{\mathrm{el}})_n} \int_{Q_n^e} \delta \left(\frac{\partial \mathbf{W}_h}{\partial z} \cdot \frac{\partial \mathbf{U}^h}{\partial z} + \frac{\partial \mathbf{W}^h}{\partial r} \cdot \frac{\partial \mathbf{U}^h}{\partial r} \right) \mathrm{d}Q = \int_{(P_n)_{\mathrm{H}}} \mathbf{W}^h \cdot \mathbf{H}^h \, \mathrm{d}P. \qquad (38)
\end{aligned}$$

A solution to this equation is developed in a manner analogous to that of equation (36). The definition of the discontinuity-capturing coefficient δ is modified slightly from that of Reference 6 for axisymmetric problems.[25] Also, the definition of $\nabla \mathbf{w}^h : \mathbf{E}^h$ in equation (38) is given in Reference 25.

3.3. Linear Elastodynamics

In the simulation of linear elastodynamics problems a semidiscrete finite element method is used in which the spatial domain is discretized using a finite element method. Analogously to the above, function spaces $\mathscr{S}_s^h$ and $\mathscr{V}_s^h$ are defined which correspond to the trial solutions and weighting functions respectively. First-order polynomials which are continuous in space are used.

The Galerkin formulation of equation (23) is: given $\mathbf{d}_0$ and $\dot{\mathbf{d}}_0$, find $\mathbf{d}^h \in \mathscr{S}_s^h$ such that $\forall \mathbf{w}_s^h \in \mathscr{V}_s^h$

$$\int_{\Omega_s} \mathbf{w}_s^h \cdot \rho_s \ddot{\mathbf{d}}^h \, d\Omega + \int_{\Omega_s} \nabla \mathbf{w}_s^h : \boldsymbol{\sigma}_s(\mathbf{d}^h) \, d\Omega = \int_{(\Gamma_s)_h} \mathbf{w}_s^h \cdot \mathbf{h}_s^h \, d\Gamma. \tag{39}$$

The finite element discretization results in a coupled system of second-order ordinary differential equations in time. This is solved using the α-method (the Hilber–Hughes–Taylor method)[26] with α set to $-0{\cdot}3$.

3.4. Interface Conditions

In the fluid–gas interaction model each element is filled completely with either gas or liquid and no phase change occurs during the simulation. The mesh moves during the simulation to track the interface and the same nodes always lie along the interface. Surface tension along the boundary is neglected so that the tractions on either side of the interface are the same. Also, the two fluids are not permitted to slip relative to each other across the interface.

The fluid model and the structure model are coupled iteratively. In each time step the structure model is updated based upon the flow data from the previous time step and the fluid model is then updated based on the new structure data. Performing two iterations between the structure and fluid models per time step results in sufficient non-linear convergence.

In computing the pressure forces upon the structure, the pressure at each surface node of the structure is computed using linear interpolation. Likewise, linear interpolation is used to compute the location of each node in the fluid mesh along the fluid–structure interface as well as the fluid velocity at that node.

4. NUMERICAL EXAMPLES

Previous work has focused on the flow characteristics of a compressible liquid propellant between pistons in relative motion in a regenerative liquid propellant gun (RLPG).[25,27] Although good comparison with experimental gun data was achieved, the simulation indicated no tendency of the flow to separate from the injection orifice boundary. Live firing tests indicate, however, that a reversal in the direction of flow between the pistons can occur. In addition, it is known that the pistons are elastic and it is speculated that the piston motion can couple to the fluid motion such that the boundary layer at the piston injection orifice is disturbed. The current fluid–elastic solid model was developed to investigate the interaction between the piston vibration and the fluid.

In addition, gas interacts with the fluid in a different region of the gun to form droplets. In this gas–fluid interaction problem, fundamental mechanisms of droplet formation can be investigated. Both problems are driven by the need to obtain fundamental physical information in regions and at pressures and temperatures where direct diagnostic data are difficult or impossible to obtain.

In order to show the applicability of these numerical models to the gun firing cycle, the models are applied to three test problems. The first is the vibration of a metal plate, both in a vacuum and also with fluid on one side of it. This problem was chosen to test the accuracy of the fluid–structure interaction model. The second problem involves the flow of liquid propellant between two pistons. The third problem involves a jet of hot gas striking a puddle of propellant.

4.1. Vibration of a flat plate

This problem was chosen to validate the fluid–structure interaction model introduced in this paper. Analytical values are available for the natural frequencies of a simply supported, round, flat plate vibrating in a vacuum and with a fluid on one side.[28] An axisymmetric model of the plate and fluid is used to compute the natural frequencies and the numerical model is validated by the comparison of the computed and analytical natural frequencies.

The simply supported boundary condition is approximated by fixing to zero the axial and radial displacements of the node in the middle of the outer boundary of the plate. A fully unstructured mesh of the plate, consisting of 866 elements and 488 nodes, is used and was generated using an automatic mesh generator developed at the Army HPC Research Center, University of Minnesota.[21]

Typically, linear triangular elements are not used for studying the dynamics of linearly elastic bodies in cases where one body dimension is much smaller than the others. This is because the displacement within a three-node triangular element is linear, so the strain within each element is approximated as constant. However, the interface conditions used in this work are much easier to implement if there is one node of the plate mesh on the fluid–structure for every node of the fluid mesh on the interface and if the plate node and the corresponding fluid node are at the same location. Also, accurate computation of the fluid dynamics requires a certain level of refinement of the mesh, and using a refined mesh of the plate is inexpensive relative to using a refined mesh of the fluid. Based on all of this, a finer mesh of the plate is used in this research than would typically be used in the study of a vibrating plate. In this mesh, with at least three elements across the plate thickness (and in most place four to six elements), the piecewise constant strain through the place thickness is sufficient to accurately model the plate.[29]

Another problem with using triangular elements to model elastic solids is that they can lock in bending. This is seen when the radial length of the element is comparable with or larger than the plate thickness. Owing to the mesh refinement in this problem, locking is not seen.[29]

The plate is initially deformed, the initial shape being determined by imposing a motion perpendicular to the plate. The magnitude of the initial displacement of a point on the plate is a sinusoidal function of the distance of the point from the symmetry axis; see Figure 1. In this figure the nodes on the outer boundary (shown at the top of Figure 1) are not displaced, but this is only a feature of the initial displacement. As the plate vibrates, only the middle node on that boundary is fixed, the other nodes on that boundary being free to move axially and radially. The plate is released from this initial shape and allowed to vibrate. Various axisymmetric natural modes of the plate are excited depending upon the initial deformation.

The plate is allowed to vibrate in a vacuum and also with a semi-infinite column of fluid on one side of that plate. The natural frequencies of vibration of this plate both with and without the liquid are given in Reference 28. In the current work, only the axisymmetric modes are being investigated.

The plate is made of 17-4 stainless steel with a Young's modulus of 196·0 GPa, a Poisson's ratio of 0·3 and a density of 7772 kg m^{-3}. It has a thickness of 4·0 cm and a radius of 1·0 m.

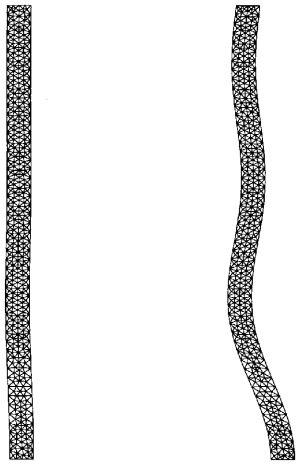

Figure 1. Vibration of a flat plate. Initial deformation of flat plate in order to measure frequency of first four axisymmetric modes (left). Initial deformation multiplied by 10 (right). Half of cross-section of plate is shown

4.1.1. Vibration of a flat plate in a vacuum. According to Reference 28, the frequencies of the first axisymmetric modes of the plate vibrating in a vacuum are 48, 288, 718 and 1338 Hz. In order to excite these modes of vibration, the plate is initially deformed and released.

The motion of the centre point of the plate during 20 ms and the data from a fast Fourier transform (FFT) of the motion of this point over a time period of approximately 0·4 s are shown in Figure 2. The motion of the plate centre point during the span $t = 0{\cdot}35$–$0{\cdot}37$ s is representative of the motion of that point during the entire simulation. The displacement of the plate centre point at $t = 0{\cdot}0$ s is 0·006 m, so the amplitude of the plate vibrations is not diminishing over time.

The computed natural frequencies of the first four axisymmetric modes, as shown in Figure 2, are 49, 295, 732 and 1348 Hz. All computed results are within 2·4% of the theoretical results.

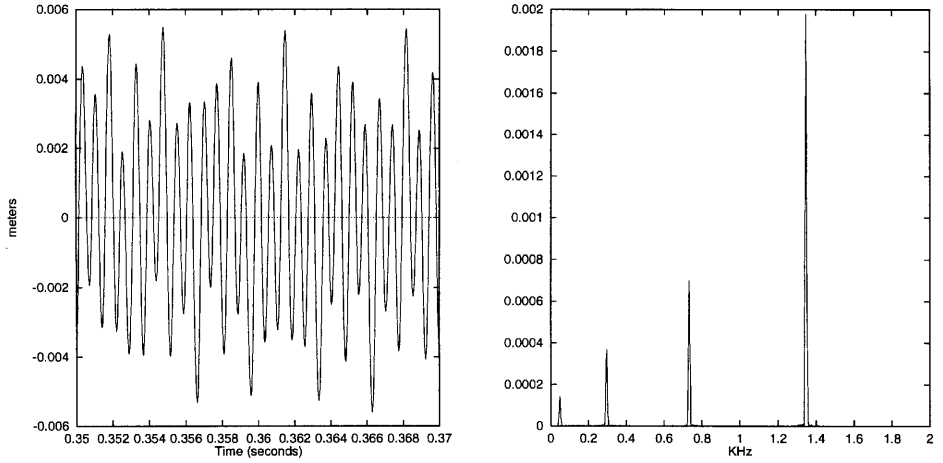

Figure 2. Vibration of a flat plate in a vacuum. Motion of centrepoint of plate (left). Frequency spectrum of plate centrepoint motion over 0·4 s (right). Plate radius 1 m, plate thickness 4 cm

4.1.2. Vibration of a flat plate with a fluid on one side. The plate was also allowed to vibrate with a fluid on one side of it. The frequency of the first axisymmetric mode of this fluid–structure problem is given in Reference 30. An unstructured mesh for the fluid was generated using the same mesh generator as above. The mesh consists of 1968 nodes and 3774 elements. The fluid used is XM46, a liquid monopropellant being studied by the U.S. Army for possible use in future field artillery weapons. The density of XM46 is 1430 kg m^{-3}. The values for equation (9) are $K_1 = 5{\cdot}35$ GPa and $K_2 = 9{\cdot}11$. According to Reference 30, the frequency of the first axisymmetric mode is 20 Hz.

In simulating this problem, the oscillation of the plate damped out fairly quickly; see Figure 3. This is due to propagation of the initial energy of the system out of the computational domain through the liquid. In the physical problem, assuming the fluid domain extends to infinity, the initial potential energy stored in the deformed plate eventually all propagates to infinity through the fluid. An FFT of the curve in Figure 3 shows a strong frequency at 19·8 Hz and a weaker frequency at 194 Hz, the computed natural frequencies for the first two axisymmetric modes. The computed frequency of the first mode is within 1% of the expected value.

Remark. The vibrating flat plate was also studied with a coarser plate mesh (250 nodes and 394 elements, with three nodes across the plate thickness) and a coarser fluid mesh (597 nodes and 1087 elements). For the plate vibrating in a vacuum the computed natural frequencies were 49, 305, 759 and 1397 Hz, all within 6% of the analytical results. For the plate with a fluid on one side the computed natural frequency was 18·3 Hz, within 8·5% of the expected value.

4.2. Vibration of a moving mechanical component

This problem was chosen to test the features of the fluid–structure interaction model. Again the problem is assumed to be axisymmetric. There is a fixed, rigid circular cylinder and a moving, deformable piston surrounding it; see Figure 4. There is a grease layer between the piston and the outer wall to prevent contact between the surfaces. Since the grease layer only needs to be 0·15 mm thick, relative to a piston outer radius of 3·75 cm, the grease layer is neglected in the calculations. The grease layer, however, imposes the pressure in the chamber onto the outer face of the piston. In order to account for this, the pressure which is imposed at the fluid outflow boundary is also imposed onto the outer face of the piston.

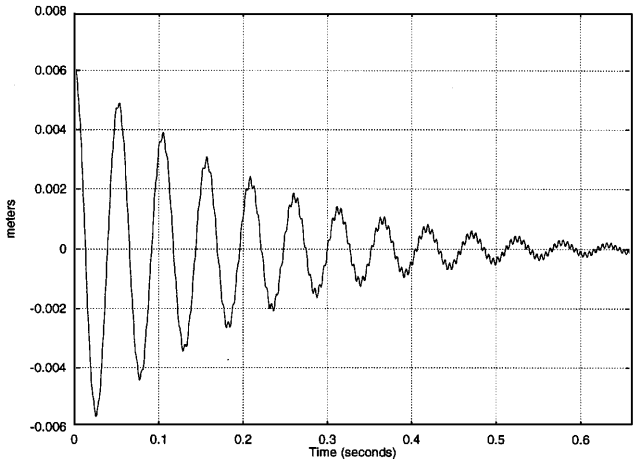

Figure 3. Vibration of a flat plate with fluid on one side. Motion of centrepoint of plate

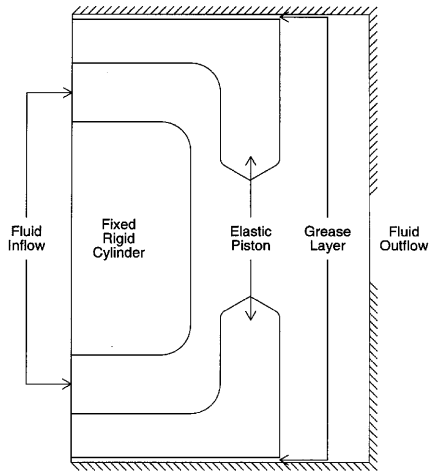

Figure 4. Vibration of a moving mechanical component. Cross-section of domain (grease layer thickness not drawn to scale)

XM46 flows in through the boundary at the left end of the domain, through the orifice at the right end of the piston and out through a circular hole in the right-hand boundary. Unstructured meshes are used for both the fluid and piston problems, again generated using the AHPCRC mesh generator. The initial mesh for the fluid and the mesh for the piston are shown in Figure 5. The mesh of the piston consists of 1382 nodes and 2570 elements and the initial fluid mesh consists of 2489 nodes and 4696 elements.

The left end of the piston is held fixed and the computations start. The piston begins to vibrate owing to the pressure forces acting upon it. Using this as an initial condition, the left end of the piston undergoes a known sinusoidal motion with an amplitude of 0·015 m and a frequency of 3 kHz. Assuming no deformation of the piston for a moment, the clearance between the piston face and the rigid cylinder end in the initial configuration is 0·5 m, which is also the maximum clearance as the piston is moved. The minimum clearance, still assuming rigid motion of the piston, is 0·002 m. With such a large difference between maximum and minimum clearances, the mesh spanning the gap between the piston and the cylinder is deformed during the simulation. To prevent excessive distortion, a new mesh is generated periodically during the stimulation. The AHPCRC mesh generator is used to generate the new meshes.

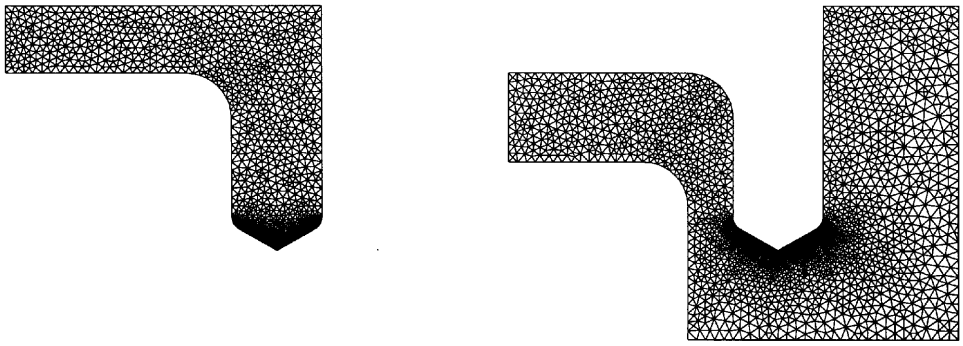

Figure 5. Vibration of a moving mechanical component. Mesh of piston (left) and fluid mesh (right)

The motion of the piston tip, the point on the piston where the radius is the smallest, relative to the left end of the piston, was chosen as a measure of the deformation of the piston. This relative motion is shown in Figure 6 along with the imposed motion on the left end of the piston. Immediately preceding the imposed sinusoidal motion, an impulsive motion is imposed to excite vibrations of the piston. In Figure 6 the initial relative motion is very oscillatory owing to this excitation. Most of the oscillations damp out quickly, leaving a few strong frequencies. The data from an FFT of this relative motion is shown in Figure 7. There are large 3 kHz oscillations, caused by the forcing function, and also oscillations near 6, 9, 12 and 15 kHz, all of which are overtones of the forcing frequency, caused by the interaction with the liquid. The oscillations near 13·5 kHz indicate that 13·5 kHz is probably a natural frequency of the piston.

The velocity vectors and Mach number distribution are shown in Plate 1. The times shown, $t = 1{\cdot}0$, 1·08, 1·17, 1·25 and 1·33 ms, span one period of the forced motion of the left of the piston.

4.3. Gas Impinging on a Liquid

The combustion rate in the RLPG is highly related to the droplet sizes formed in both initial and final ignition processes. Droplet formation mechanism involved in the initial ignition process are roll wave, wave undercut, bubble burst and liquid impingment. In each mechanism, very complicated gas–liquid interactions occur which result in an unstable interface between the gas and liquid.

In the initial ignition process of the RLPG the droplets are formed predominantly by roll wave and wave undercut mechanisms. In these mechanisms a sufficiently high gas velocity makes the gas–liquid interface unstable and waves appear. Droplets are formed in the regions where the shear forces are larger than the surface tension. Therefore one can split the wave undercut mechanism into two parts, i.e. wave formation and droplet formation.

The objective of this problem is to demonstrate the computational capability of simulating wave formation. This capability will be used to obtain a better understanding of the fundamental physics behind wave formation caused by the wave undercut mechanism and the subsequent formation of droplets. In this problem, incompressible gas with a velocity of 50 m s^{-1} at an angle of 30° from the vertical hits flammable liquid which is initially at rest. Initially the liquid occupies the lower quarter of a cube with dimensions 10 cm on each side. The liquid is assumed to be 45·3 times heavier than the gas and the Reynolds number based on the cube size, injection velocity and viscosity of the gas is 10^6. The computation is carried out on the parallel supercomputer Thinking Machines CM-5 using a

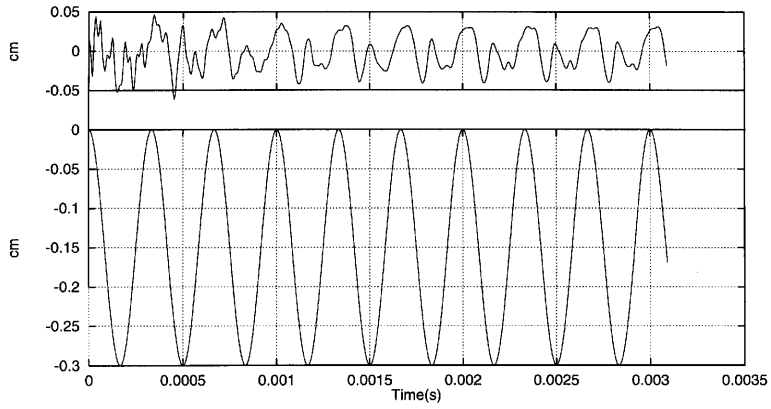

Figure 6. Vibration of a moving mechanical component. Imposed motion on left end of piston (bottom). Motion of tip of piston in orifice, relative to left end of piston (top) (negative indicates motion towards fixed block)

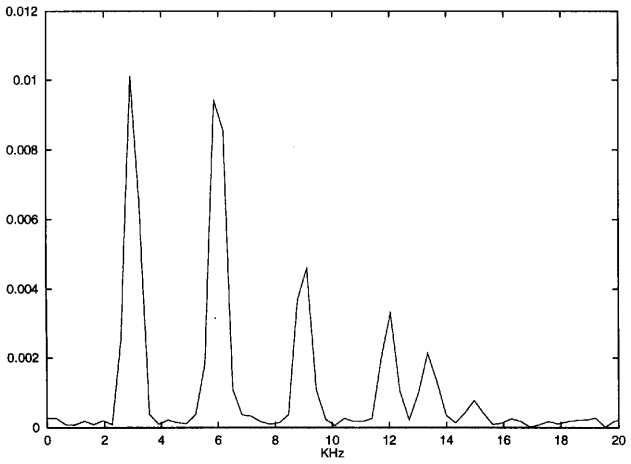

Figure 7. Vibration of a moving mechanical component. Frequency spectrum of motion of piston tip relative to left end of piston

structured mesh made of $50 \times 50 \times 50$ hexahedral elements. The time increment was set to 0·05 and in every time step approximately 10^6 coupled non-linear equations are solved to obtain the pressure and velocity fields. To keep track of the interface between the gas and liquid, we use an automatic mesh-moving scheme to move the finite element mesh. The mesh-moving scheme, which is based on the linear elasticity equations, is described in Reference 20. Using this scheme, more than 400,000 equations are solved to update the finite element mesh at every time step.

Plate 2 shows the velocity field in the vertical, central plane (left picture) and the pressure distribution on the surface of the liquid (right picture) at $t = 0{\cdot}05$ s. Figure 8 shows the surface of the liquid at $t = 0{\cdot}0$ s (left picture) and $t = 0{\cdot}075$ s (right picture).

5. CONCLUSIONS

The deformable-spatial-domain/stabilized-space–time (DSD/SST) formulation has been successfully applied to problems involving fluid–structure interactions and two-fluid interfaces. Specifically, we have demonstrated the capability to model the coupled behaviour of a piston behaving as an elastic solid and a compressible fluid in which the computational domain must be determined as part of the calculation as it changes in size and shape. Although few data are available for validation, the reliability of the method is first demonstrated by comparison with a problem involving a flat plate. In

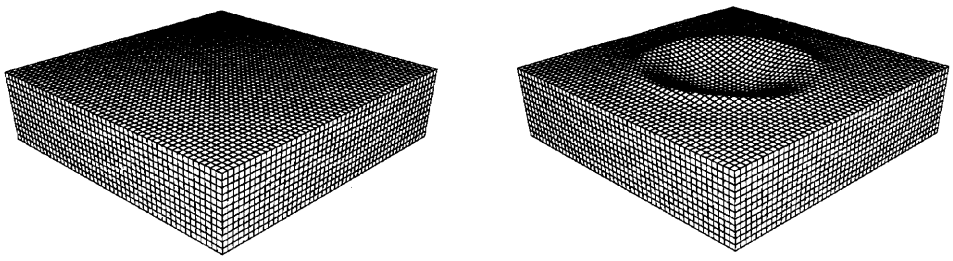

Figure 8. Gas impinging on a liquid. Surface discretization of liquid at $t = 0{\cdot}0$ s (left) and $t = 0{\cdot}075$ s (right)

addition, we have modelled the interaction at the interface of an ideal gas and a barotropic fluid in which the gas impinges on the liquid.

The modelling capabilities discussed are of interest to the U.S. Army in the investigation of physical behaviour encountered in advanced weapons systems. Since experimental diagnostics are often difficult or impossible at the extremes of conditions encountered in guns, high-fidelity models often provide the primary means of understanding the dominant physical mechanisms at gun pressures and temperatures.

ACKNOWLEDGEMENTS

The unstructured mesh generator used in this work is courtesy of Andrew Johnson, AHPCRC, University of Minnesota. This research was sponsored by NASA-JSC under grant NAG 9-449 and by ARPA under NIST contract 60NANB2D1272. This work was also sponsored in part by the Army High Performance Computing Research Center under the auspices of the Department of the Army, Army Research Laboratory co-operative agreement number DAAH04-95-2-0003/contract number DAAH04-95-C-0008, the content of which does not necessarily reflect the position or the policy of the government, and no official endorsement should be inferred. Support for the third author and CRAY C90 time were provided in part by the Minnesota Supercomputer Institute. This work was supported in part by a grant of HPC time from the DoD HPC Center, Vicksburg Center, CRAY C90.

REFERENCES

1. C. Johnson, U. Navert and J. Pitkäranta, 'Finite element methods for linear hyperbolic problems', *Comput. Methods Appl. Mech. Eng.*, **45**, 285–312 (1984).
2. T. J. R. Hughes and G. M. Hulbert, 'Space–time finite element methods for elastodynamics: formulations and error estimates', *Comput. Methods Appl. Mech. Eng.*, **66**, 339–363 (1988).
3. F. Shakib, 'Finite element analysis of the compressible Euler and Navier–Stokes equations', *Ph.D. Thesis*, Department of Mechanical Engineereing, Stanford University, 1988.
4. P. Hansbo and A. Szepessy, 'A velocity–pressure streamline diffusion finite element method for the incompressible Navier–Stokes equations', *Comput. Methods Appl. Mech. Eng.*, **84**, 175–192 (1990).
5. T. E. Tezduyar, M. Behr and J. Liou, 'A new strategy for finite element computations involving moving boundaries and interfaces—the deforming-spatial-domain/space–time procedure: I. The concept and the preliminary tests', *Comput. Methods Appl. Mech. Eng.*, **94**, 339–351 (1992).
6. S. K. Aliabadi and T. E. Tezduyar, 'Space–time finite element computation of compressible flows involving moving boundaries and interfaces', *Comput. Methods Appl. Mech. Eng.*, **107**, 209–224 (1993).
7. T. Tezduyar, S. Aliabadi, M. Behr, A. Johnson and S. Mittal, 'Massively parallel finite element computation of three-dimensional flow problems', *Proc. 6th Jpn. Numerical Fluid Dynamics Symp.*, Tokyo, 1992, pp. 15–24.
8. T. E. Tezduyar, S. K. Aliabadi, M. Behr and S. Mittal, 'Massively parallel finite element simulation of compressible and incompressible flows', *Comput. Methods Appl. Mech. Eng.*, **119**, 157–177 (1994).
9. S. Mittal and T. E. Tezduyar, 'Massively parallel finite element computation of incompressible flows involving fluid–body interactions', *Comput. Methods Appl. Mech. Eng.*, **112**, 253–282 (1994).
10. T. J. R. Hughes and A. N. Brooks, 'A multi-dimensional upwind scheme with no crosswind diffusion', in T. J. R. Hughes (ed.), *Finite Element Methods for Convection Dominated Flows*, AMD Vol. 34, ASME, New York, 1979, pp. 19–35.
11. A. N. Brooks and T. J. R. Hughes, 'Streamline upwind/Petrov–Galerkin formulations for convection dominated flows with particular emphasis on the incompressible Navier–Stokes equations', *Comput. Methods Appl. Mech. Eng.*, **32**, 199–259 (1982).
12. T. E. Tezduyar and T. J. R. Hughes, 'Finite element formulations for convection dominated flows with particular emphasis on the compressible Euler equations', *AIAA Paper 83-0125*, 1983.
13. J. Donea, 'A Taylor–Galerkin method for convective transport problems', *Int. J. Numer. Methods Eng.*, **20**, 101–120 (1984).
14. T. J. R. Hughes and M. Mallet, 'A new finite element formulation for computational fluid dynamics: III. The generalized streamline operator for multidimensional advective–diffusive systems', *Comput. Methods Appl. Mech. Eng.*, **58**, 305–328 (1986).
15. G. J. Le Beau, S. E. Ray, S. K. Aliabadi and T. E. Tezduyar, 'SUPG finite element computation of compressible flows with the entropy and conservation variables formulations', *Comput. Methods Appl. Mech Eng.*, **104**, 397–422 (1993).

16. S. K. Aliabadi, S. E. Ray and T. E. Tezduyar, 'SUPG finite element computation of viscous compressible flows based on the conservation and entropy variables formulations', *Comput. Mech.*, **11**, 300–312 (1993).
17. S. K. Aliabadi and T. E. Tezduyar, 'Parallel fluid dynamics computations in aerospace applications', *Int. J. Numer. Methods Fluids*, **21**, 783–805 (1995).
18. T. J. R. Hughes, L. P. Franca and G. M. Hulbert, 'A new finite element formulation for computational fluid dynamics: VIII. The Galerkin/least-squares method for advective–diffusive equations', *Comput. Methods Appl. Mech. Eng.*, **73**, 173–189 (1989).
19. M. Behr and T. E. Tezduyar, 'Galerkin/least-squares space–time finite element method for deforming domains—recent developments', *Proc. BAIL VI Conf.* 1992.
20. A. A. Johnson and T. E. Tezduyar, 'Mesh update strategies in parallel finite element computations of flow problems with moving boundaries and interfaces', *Comput. Methods Appl. Mech. Eng.*, **119**, 73–94 (1994).
21. A. A. Johnson, 'Mesh generation and update strategies for parallel computation of flow problems with moving boundaries and interfaces', *Ph.D. Thesis*, Department of Aerospace Engineering and Mechanics, University of Minnesota, 1995.
22. A. A. Johnson and T. E. Tezduyar, 'Parallel computation of incompressible flows with complex geometries', *Int. J. Numer. Methods Fluids*, **24**, 1321–1339 (1997).
23. J. D. Achenbach, *Wave Propagation in Elastic Solids*, North-Holland, New York, 1973.
24. S. Mittal and T. E. Tezduyar, 'A finite element study of incompressible flows past oscillating cylinders and airfoils', *Int. J. Numer. Methods Fluids*, **15**, 1073–1118 (1992).
25. S. E. Ray, 'Large-scale computational strategies for solving compressible flow problems', *Ph.D. Thesis*, Department of Aerospace Engineering and Mechanics, University of Minnesota, 1995.
26. T. J. R. Hughes, *The Finite Element Method. Linear Static and Dynamic Finite Element Analysis*, Prentice-Hall, Englewood Cliffs, NJ, 1987.
27. G. P. Wren, S. E. Ray, S. K. Aliabadi and T. E. Tezduyar, 'Space–time finite element computation of compressible flows between moving components', *Int. J. Numer. Methods Fluids*, **21**, 981–991 (1995).
28. R. D. Blevins, *Formulas for Natural Frequency and Mode Shape*, Van Nostrand Reinhold, New York, 1979.
29. H. K. Stolarski, personal communication, 1996.
30. W. H. Peak and E. G. Thurston, 'The lowest resonant frequency of a water-loaded circular plate', *J. Acoust. Soc. Am.*, **26**, 166–168 (1954).

